AIP Review of Scientific Instruments

Design of a beamline for soft and deep lithography on third generation synchrotron radiation source

E. Di Fabrizio, A. Nucara, M. Gentili, and R. Cingolani

Citation: Review of Scientific Instruments 70, 1605 (1999); doi: 10.1063/1.1149640
View online: http://dx.doi.org/10.1063/1.1149640
View Table of Contents: http://scitation.aip.org/content/aip/journal/rsi/70/3?ver=pdfcov
Published by the AIP Publishing

Articles you may be interested in
The infrared synchrotron radiation beamline at the third generation light source ELETTRA
Rev. Sci. Instrum. **74**, 3934 (2003); 10.1063/1.1602959

The design and performance of an x-ray micro-focusing system using differentially deposited elliptical mirrors at the National Synchrotron Light Source
Rev. Sci. Instrum. **73**, 3464 (2002); 10.1063/1.1505656

Bending-magnet beamline for x-ray microtechniques at the Advanced Photon Source (abstract)
Rev. Sci. Instrum. **73**, 1550 (2002); 10.1063/1.1448165

Recent design upgrades of the APS beamline standard components
Rev. Sci. Instrum. **73**, 1584 (2002); 10.1063/1.1435818

Performance of the advanced photon source 1-BM beamline optics
Rev. Sci. Instrum. **70**, 4457 (1999); 10.1063/1.1150096

This article is copyrighted as indicated in the article. Reuse of AIP content is subject to the terms at: http://scitationnew.aip.org/termsconditions. Downloaded to IP: 132.204.37.217 On: Wed, 10 Dec 2014 17:51:20

Design of a beamline for soft and deep lithography on third generation synchrotron radiation source

E. Di Fabrizio[a)]
INFM-TASC at Elettra Synchrotron Lightsource-Lilit Beamline S.S. 14 KM 163.5, Area Science Park, 34012 Basovizza-Trieste (Italy)

A. Nucara
INFM, Dipartimento di Fisica, Universita' di Roma La Sapienza, 00185 Roma, Italy

M. Gentili
Istituto Elettronica Stato Solido, via Cineto Romano, 42 00156 Roma, Italy

R. Cingolani
INFM, Dipartimento Scienze dei Materiali Via Arnesano, Universita' di Lecce, 73100 Lecce, Italy

(Received 8 October 1998; accepted for publication 1 December 1998)

ELETTRA is a third generation synchrotron radiation source. The energy spectrum allows the design of beamlines suitable for x-ray lithography from soft to hard x-ray wavelengths. An appropriate lithographic window for micro- and nanofabrication can be obtained by a combination of selected filters and mirrors. As the beamline is interfaced to a vertical x-ray stepper, a uniformity in the beam intensity better than 3% (3σ) in the horizontal direction has to be reached. The present beamline is designed by taking into account the main factors which can affect the beam quality, namely, thermal loading on mirrors and filters, slope errors, and surface roughness of the mirrors. The resulting lithographic resolution at soft x-ray wavelengths is better than 100 nm. © *1999 American Institute of Physics.* [S0034-6748(99)02303-5]

I. INTRODUCTION

In this article we present a complete design of a lithographic beamline working from soft (1.5 keV) to hard (10 keV) x rays to be installed on a third generation synchrotron. In particular, the design is referred to ELETTRA, the synchrotron radiation facility operating at Trieste (Italy).[1] Synchrotrons of the third generation are optimized for the use of insertion devices such as wigglers and undulators, but some of their characteristics are advantageous even for lithographic beamlines based on bending magnets. The high brightness of the electron beam makes it possible to collect intense photon flux with only a few milliradians of horizontal acceptance. As a consequence, the source is symmetric in the horizontal plane so that the lithographic image can be optimized by using one toroidal mirror and avoiding the complex aspherical optics used for asymmetric sources with high horizontal acceptance (>30 mrad).[2] Another advantage of the high brightness is that the divergence of the beam at the focal plane gives small runout. The field distortions on the mask/wafer plane is then in the range of few nanometers, a value compatible with a high placement accuracy (<20 nm).[3] Finally, the intensity distribution at the mask/wafer plane is uniform within 3% (3σ). This uniformity is needed when using high sensitivity resist for high throughput processes.[4]

This article includes a comparative study of two beamline configurations distinguished by different mirror arrangements. The difference between the two cases is the relative location of the plane mirror with respect to the toroidal one. The design includes a study of the impact of the slope error of the mirrors on the expected lithographic image, as well as the calculation of the downstream power from the source to the mask/wafer plane at the exposure station. A comparative study of the thermal properties of a SiO_2 and a Si mirror has also been performed.

The peculiarity of the present design consists mainly of its wide lithographic window. This is achieved by combining high-pass filters (beryllium windows or other suitable materials) with low-pass filters (mirrors at increasing angles of incidence). Our design allows the continuous change of the spectral range of interest from the soft to hard x-ray region. While in the soft x-ray range (photon energy between 1 and 2 keV) one achieves the highest lithographic resolution, in the hard x-ray region (photon energy higher than 5 keV) sensitive materials of thickness of tens of microns can be exposed.

Many new applications can be envisaged both at hard and soft x rays, such as fabrication of hard x-ray optics,[5] micromachining devices,[6] photonic band-gap crystals,[7] and SiO_2 refractive index modulation,[8] quantum wires and quantum dots devices.[9] Quantum wires, quantum dots, and photonic band-gap arrays with high filling factor can be implemented as active layers of novel photonic and optoelectronic structures. State-of-the-art quantum wires and quantum dots are presently fabricated by epitaxial regrowth on periodically patterned semiconductor substrates. The intrinsic limitation of the current technology lies in lithographic processes which do not allow high-density patterning by optical methods. X-ray proximity lithography allows fabrication of high

[a)]Electronic mail: difabrizio@iess.rm.cnr.it

 © 1999 American Institute of Physics
This article is copyrighted as indicated in the article. Reuse of AIP content is subject to the terms at: http://scitationnew.aip.org/termsconditions. Downloaded to IP: 132.204.37.217 On: Wed, 10 Dec 2014 17:51:20

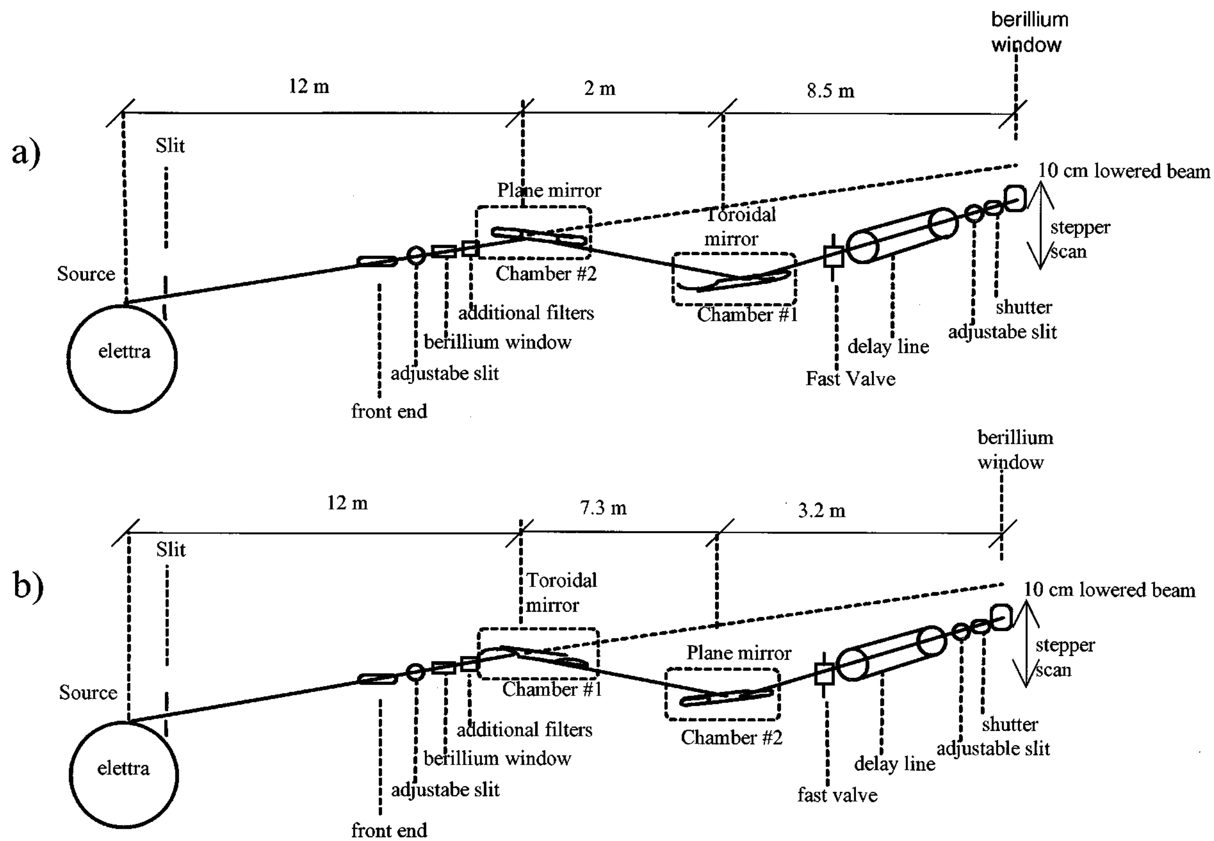

FIG. 1. Optical layout for the lithographic beamline (a) layout A: plane mirror+toroidal mirror, (b) layout B: toroidal mirror+plane mirror.

density quantum wire and quantum dot arrays over large areas, with high reproducibility and considerable benefits with respect to the time consuming electron-beam lithography (over small areas). The fabrication of high density heterostructures is a primary requirement if one wants to overcome the main limitations of present nanodevices. This will produce high gain quantum dot/wire optical devices for photonic applications (lasers, nonlinear optical modulators, etc.). Similar challenges are encountered in the fabrication of photonic band-gap structures for visible radiation, one of the major tasks of future photonic research.[10] The approach described above could be easily extended to photonic band-gap structures. An increasing demand for small periodicity gratings is invading the market for the realization of blue and ultraviolet distributed feedback and surface emitting lasers (based on GaN or II–VI materials), which represent the technology of choice for short-wavelength optical memory devices. Any technology developed to produce high-density quantum-wire arrays could also be applied to the fabrication of ultrafine gratings.

In this article in Sec. II we describe the possible beamline layouts and their performances in terms of transmittance. In Sec. III we discuss the optimization of the image, as obtained by ray-tracing simulations. Section IV is devoted to a study of the thermal load of the optical elements and the consequent effect on the lithographic image. In the Sec. V and the last section we discuss the performances of two different layouts for lithographic applications. We will also discuss the three main figures of merit of the exposure processes in lithography: resolution, placement, throughput. For soft lithography all of them are important, while in deep lithography the first two quantities are less critical than the third one.

TABLE I. Values of the grazing angles on M1 and M2 for both layouts.

Layout A			Layout B		
Mirror 1 θ_1 (deg)	Mirror 2 Height (cm)	θ_2 (deg)	Mirror 1 θ_1 (deg)	Mirror 2 Height (cm)	θ_2 (deg)
2.8	−17.49	2.75			
1.8	−12.58	1.89	1	−20.25	1.9
1.5	−10.48	1.52	0.8	−16.2	1.35
1	−6.98	0.9	0.5	−10.12	1
0.7	−4.89	0.53	0.27		no mirror
0.28	No mirror	No mirror			

II. GENERAL DESCRIPTION OF THE BEAMLINE LAYOUTS

Two optical layouts have been studied for this beamline. Layout A, as seen in Fig. 1(a) consists of one plane mirror (M1) placed at 12 m from the source and of a second toroidal mirror (M2) placed at 2 m from M1. The total length of the beamline, calculated from the front end port, is 12 m. Layout B [Fig. 1(b)] has an identical geometry, but mirror M1 is toroidal and M2 is plane. The distance between the mirrors in layout B is 7.3 m. The total length of the beamline in B is 12 m.

This article is copyrighted as indicated in the article. Reuse of AIP content is subject to the terms at: http://scitationnew.aip.org/termsconditions. Downloaded to IP: 132.204.37.217 On: Wed, 10 Dec 2014 17:51:20

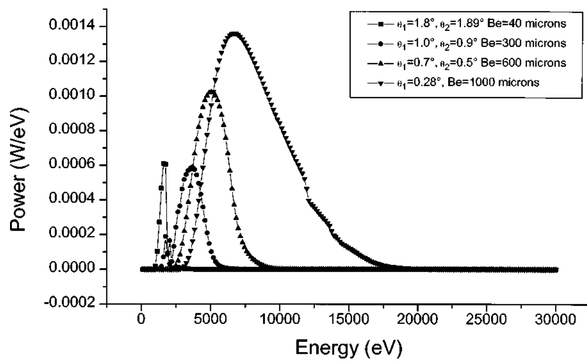

FIG. 2. Calculated transmission spectra of the beamline for different values of the incidence angles. The absorption from two beryllium windows of various thicknesses is included in the calculation.

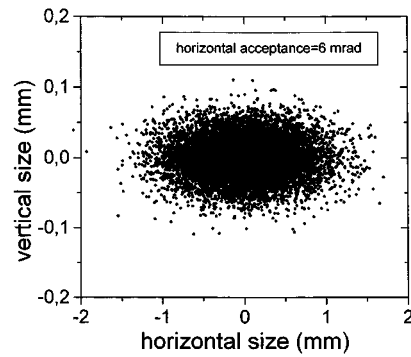

FIG. 3. Map of the synchrotron radiation emitted by a bending magnet of ELETTRA, as simulated with SHADOW.

As shown in Fig. 1 an adjustable slit, a beryllium window and an additional filter are located before M1. The adjustable slit selects the solid angle under which the synchrotron radiation is collected. As will be discussed later, the collection angles have been fixed at 6 mrad in the horizontal plane and 0.83 mrad in the vertical plane. The latter value corresponds to the natural divergence of the synchrotron radiation in the soft x-ray range under the standard operating condition of the beamline. An adjustable slit, a photon shutter, and a second beryllium window are placed after M2.

The geometrical constraints to the optical design are: (i) the height from the ground of the image; (ii) the size of the image.
The optical system has to produce an image of the source at the wafer/mask location whose size is $V \times H = 3 \times 50\,\text{mm}^2$ ($V \times H$ stands for vertical by horizontal size). This is lowered by about 10 cm from the optical axis. According to constrain (i), both layouts can operate at several grazing angles on M1 and M2 (θ_1, θ_2). Selected values of θ_1 and θ_2 are reported in Table I. These values cover a spectral region wider than the standard lithographic window[11] (1.5–12 keV). The better resolution is reached at lower energy (higher θ_1, θ_2). At higher energies for deep lithography, where lower resolution is needed[12] the image quality becomes poorer. Figure 2 displays the spectra of the beamline for layout A, as a function of angles θ_1 and θ_2. As shown in Fig. 2, the spectral region of interest can be selected by varying the optical and geometrical parameters. The second geometrical constraint (ii) can be fulfilled by a suitable choice of the mirror curvature parameters, as will be discussed in the next section.

TABLE II. Selected beam and ring parameters of ELETTRA.

Beam energy	2 GeV
Bending magnet field	1.2 T
Average ring current	300 mA
Horizontal emittance	7 nm rad
Vertical emittance	0.7 nm rad
Horizontal e-beam dimension (rms)	371 μm
Vertical e-beam dimension (rms)	43 μm
Horizontal rms divergence	698 μrad
Vertical rms divergence	14 μrad
Critical energy	3.2 keV
Bending magnet radius	5.5 m

III. RAY TRACING SIMULATION

A. Synchrotron source

The ray tracing simulation was performed using the SHADOW code.[13] The bending magnet source was simulated with the ring parameters of ELETTRA[14] and reported in Table II. We consider 6 mrad for the horizontal acceptance angle and 0.83 mrad (the natural divergence in the x-ray energy domain) for the limiting vertical spread. The value of the horizontal divergence, due to the ELETTRA design, is smaller than the usual values adopted in the lithographic beamlines operating in synchrotrons of a previous generation.[11] Due to the small divergence, of the the photon beam, the synchrotron source is symmetric (see Fig. 3) and it can be imaged by a toroidal mirror of medium size. Moreover, the high brightness of ELETTRA guarantees a high flux beamline.

B. Beamline

Figure 4 shows the images at the entrance slit of the exposure station (stepper) for two selected optical configurations of layouts A and B. The exit slit of the beamline has a rectangular shape whose vertical and horizontal sizes are $V \times H = 7 \times 50\,\text{mm}^2$. The sagittal and meridional radii of curvature ρ and R of the toroidal mirror are obtained from the Coddington's equations:[15]

$$\rho = \frac{2pq\sin\beta}{p+q}, \tag{1}$$

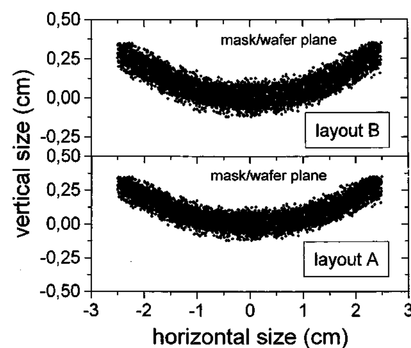

FIG. 4. Images produced by both layouts A and B at the mask/wafer plane.

This article is copyrighted as indicated in the article. Reuse of AIP content is subject to the terms at: http://scitationnew.aip.org/termsconditions. Downloaded to IP: 132.204.37.217 On: Wed, 10 Dec 2014 17:51:20

TABLE III. Image size and radii of curvature for the toroidal mirror of layouts A and B.

Layout	Vertical size (mm)	Horizontal size (mm)	R (m)	ρ (m)
A	2	50	340	0.55
B	2	50	719	0.31

$$R = \frac{2pq}{(p+q)\sin\beta}, \tag{2}$$

where p is the distance between the source and the mirror, q is the distance between the mirror and the focal point, and β is the glancing angle.

Assuming that the wafer is located at a distance L from the mirror, and that the horizontal size of the beam at L is w, the distance q is given by

$$q = \frac{pL}{p-(w/tg\,\alpha)}, \tag{3}$$

where α is the total divergence of the photon beam impinging on the mirror.

In Table III we report the values of the image size at the wafer plane, and the resulting mirror radii obtained for configurations of lowest θ_1 and θ_2 values in Table I. The mirror parameters have been chosen in order to optimize the image in the soft x-ray spectral region (photon energy ~1.5 keV), where the highest resolution is required. However, the beamline can operate at photon energies higher than 4 keV for deep lithography. In the latter case, even if the image quality is poorer, the required resolution is lower than that needed for soft x-ray lithography.
The size of the mirrors obtained by the simulation for both layouts is $65\times 10\,\mathrm{cm}^2$. Figure 5 shows the size of both the plane and the toroidal mirror, as well as the footprint of the rays impinging on their surfaces for layout A.

Figure 6 shows the runout and penumbral blur for both layouts A and B. We obtained a significant uniformity of the horizontal angular distribution at the wafer location, whose limits are ±2.5 mrad in the case of layout A, and ±1.1 mrad for layout B. The exposure field distortion is compatible with the standard design rules for devices of critical dimensions in the sub-100 nm range.[16] Figure 7 finally shows the intensity distribution of the image on the horizontal plane. The intensity distribution uniformity on a 5 cm wide exposure field is better than 3% (3σ) when 10^6 rays used for the simulation. This value confirms the high uniformity of the beam at the wafer location.

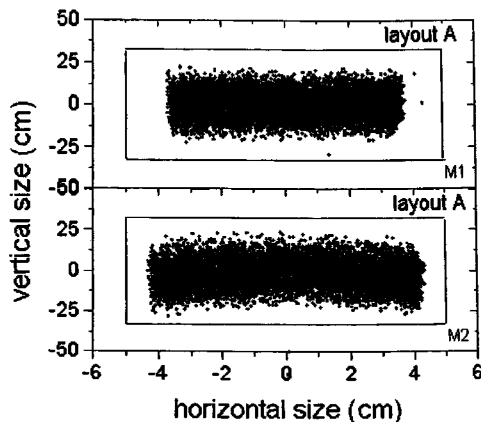

FIG. 5. Illumination of the mirrors M1 and M2 of layout A. The box as drawn in the figure represent the mirror surfaces.

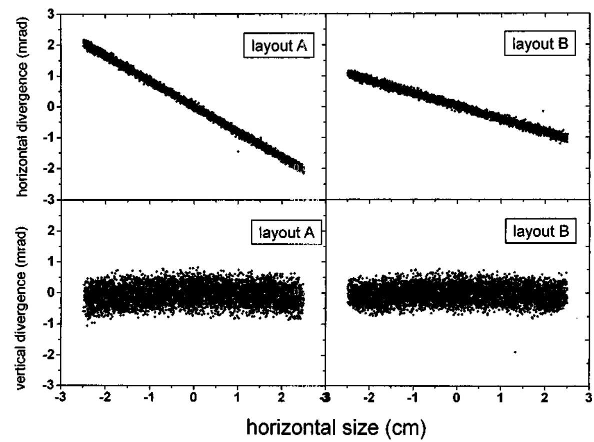

FIG. 6. Runout figure (top panels) and penumbral blur (bottom panels) for the image of the layouts A and B.

C. Mirror roughness

The influence of the mirror roughness on the quality of the image has been evaluated by three different simulations assuming an average roughness of 2, 5, and 10 Å, respectively, for gold coated mirrors (see Fig. 8). The enhancement of ray scattering induced by the increase of roughness primarily affects the average value of the intensity, whereas the uniformity of the intensity distribution does not change significantly due to the random nature of the scattering process. As shown in Fig. 8, an acceptable tradeoff between image quality and manufacturing feasibility is obtained by choosing a roughness of 5 Å.

One may notice that, even an increase of the roughness as small as 10 Å results in substantial changes of the image. This behavior is due to the Debye–Waller factor,[17] which is more sensitive to the roughness when working at small grazing angle.

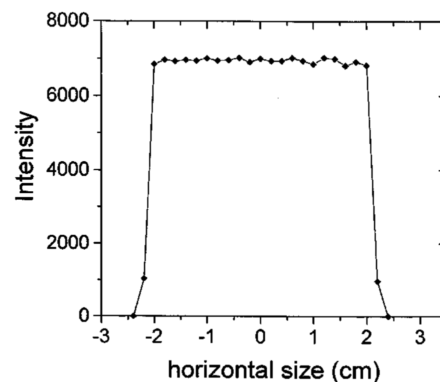

FIG. 7. Horizontal intensity distribution of the image in the mask/wafer plane. The sampling of the distribution is obtained by use of 10^6 rays.

This article is copyrighted as indicated in the article. Reuse of AIP content is subject to the terms at: http://scitationnew.aip.org/termsconditions. Downloaded to IP: 132.204.37.217 On: Wed, 10 Dec 2014 17:51:20

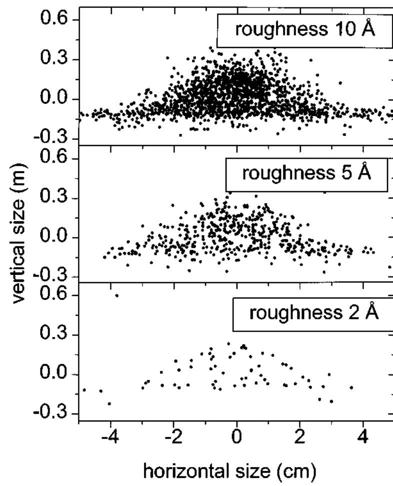

FIG. 8. Plot of the lost rays in the mask/wafer plane due to the roughness of the mirror surface coated with Au.

D. The mirror slope error

The slope error of the mirrors has also been considered in the simulation. Suitable mirror surfaces have been generated by using the SHADOW routine.[18] We tested the influence of the slope error for layout A at $\theta_1 = 88.2°$ and $\theta_2 = 88.11°$, this operating condition being the most critical from the lithographic point of view. The results are shown in Fig. 9 for selected values of the slope error. In Table IV we report the rms values of the image size resulting from the simulations. In the same table we show the horizontal (sagittal) slope error Δ_s, the vertical (meridional) slope error Δ_m and the value of the slope error Δ^* in the vertical plane seen by the radiation. The latter takes into account the incidence angle θ through the relation:

$$\Delta^* = \frac{\Delta_\nu}{\cos\theta}. \tag{4}$$

One may notice that the broadening in the horizontal plane is hidden by the large horizontal size of the image. On the contrary, the vertical size increases by a factor of 2 by varying Δ_m from 8 to 60 μrad.

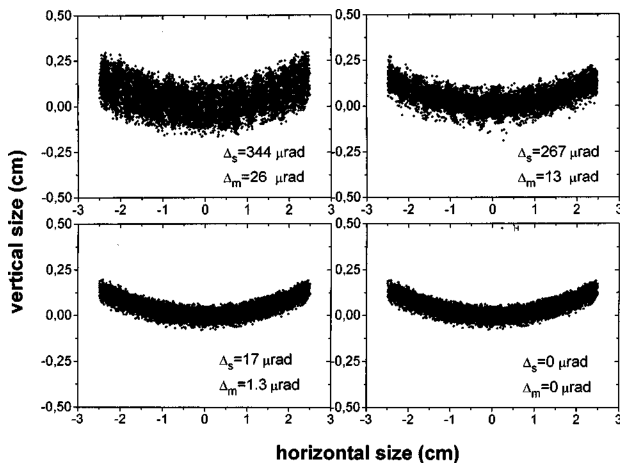

FIG. 9. Image broadening produced by layout A at the mask/wafer plane due to the mirror slope errors.

TABLE IV. Values of the slope error and rms value of the image size obtained from the simulation.

Δ_s (μrad)	Δ_m (μrad)	Δ^* (μrad)	Horizontal rms size (cm)	Vertical rms size (cm)
0	0	0	1.249	0.0586
113	8	222	1.249	0.0646
150	18	516	1.249	0.0760
339	31	888	1.249	0.0858
408	41	1175	1.248	0.100
1939	48	1375	1.246	0.104
569	58	1662	1.246	0.129

IV. THERMAL LOAD

Due to the high radiation flux, thermal load is a critical issue in synchrotrons of third generation. This may change the ideal optical surfaces, causing defocalization and dispersion of the image. In this section we estimate the thermal load on the first beryllium window and on both mirrors, and we calculate their equilibrium temperature.

The calculation of the power delivered by the synchrotron and absorbed by the optical elements (filters and mirrors) is performed by using TRANSMIT.[19]

A. Thermal load on the Be window

The thermal load on the Be window is $Q = 25\ \mathrm{W/cm^2}$ for a current 350 mA in the ring and in the soft X-ray lithography mode (see Table VI). Assuming that irradiation is the only thermal exchange mechanism, one can estimate the equilibrium temperature T^* of the Be window. In the frame of the grey-body theory[20] we consider a convex surface A_1, contained in a box of inner surface A_2. The power density Q exchanged between A_1 and A_2 is given by

$$Q = \frac{A_1 \sigma (T^{*4} - T_2^4)}{\dfrac{1}{\epsilon_1} + \dfrac{A_1}{A_2}\left(\dfrac{1}{\epsilon_2} - 1\right)}, \tag{5}$$

where σ is the Stefan–Boltzmann constant, ϵ represents the emittivity of the surfaces. T^*, and T_2 are the equilibrium temperatures. In the case of the beryllium window located at the front end, Eq. (5) can be used in the limit $A_1/A_2 \rightarrow 0$. For $Q = 25$ W and $\epsilon = 0.82$[21] one obtains $T^* = 1640$ K. This value indicates the need for water cooling the window, since the melting temperature of beryllium is $T_m = 1551$ K. Cooling could be avoided by the use of a carbon window, whose equilibrium temperature ranges between 1173 and 11273 K, (assuming $0.8 < \epsilon < 0.93$). Those values are much smaller than the melting temperature of carbon ($T_m = 3925$ K). However, a limitation to the use of carbon window for lithographic applications, arises from poor uniformity on thickness, which may affect the intensity distribution of the beam. Other filter materials, such as aluminum or copper can be used for deep lithographic applications. Also in this case water cooling is needed, due to the low melting temperature of those materials ($T_{\mathrm{Al}} = 933$ K and T_{Cu} 1357 K).

This article is copyrighted as indicated in the article. Reuse of AIP content is subject to the terms at: http://scitationnew.aip.org/termsconditions. Downloaded to IP: 132.204.37.217 On: Wed, 10 Dec 2014 17:51:20

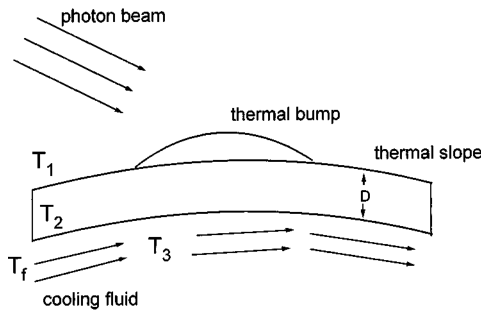

FIG. 10. Schematics of the cooling geometry, as proposed in Ref. 22.

B. Thermal load on the first mirror

In this section we consider the distortion of mirror surfaces due to the thermal load. In particular, we have studied two materials widely used for beamline optics, namely fused silica (SiO_2) and silicon (Si).

By taking into account the energy fall at the beryllium window, the absorbed power density on the first mirror M1, as calculated by TRANSMIT, turns out to be $Q = 0.1\ \mathrm{W/cm^2}$ at the lowest incidence angle. In the following we discuss the effects on the image of the M1 distortion induced by the thermal load. The power density absorbed by the M2 mirror is $Q = 0.0017\ \mathrm{W/cm^2}$, which results in a negligible distortion of the image. We will neglect this distortion in the following.

A first estimate of the additional curvature of mirror M1 is obtained following Smither,[21] and by assuming a continuous cooling by liquid water. Referring to Fig. 10, we identify two main thermal effects: a bump on the surface of the mirror exposed to the radiation and slope induced on the whole mirror. The former effect can be modeled by using a Gaussian shape for the bump, whose slope is given by

$$\Delta\theta = 1.4\left(\frac{H}{\mathrm{FWHM}}\right) \tag{6}$$

where H is the height of the bump. For a SiO_2 mirror, $H = 4\ \mu\mathrm{m}$ and full width at half maximum (FWHM) = 25 cm, so that $\Delta\theta = 22\ \mu\mathrm{rad}$. For a Si mirror of the same size, $H = 0.2\ \mu\mathrm{m}$ and $\Delta\theta = 0.1\ \mu\mathrm{rad}$. Both values of the bump obtained are compatible with the required average slope error reported in Sec. III D.

Concerning the thermal slope of the whole mirror, its radius of curvature R_t is calculated through the equation:

$$R_t = \frac{k}{\alpha Q}, \tag{7}$$

where α is the expansion coefficient and k is the thermal conductivity of the mirror. The temperature T^* of the exposed surface at thermal equilibrium is:[22]

$$T^* = \Delta T_{12} + \Delta T_{23} + \Delta T_3 + T_f, \tag{8}$$

where

$$\Delta T_{12} = T_1 - T_2 = \frac{DQ}{k}, \tag{9}$$

TABLE V. The expansion coefficient and the thermal conductivity of Si and SiO_2, together with the thermal slope radius and the equilibrium temperature.

	α (°C)$^{-1}$	k (W/cm °C)	R_t (m)	T^* (°C)
Si	4.2×10^{-6}	1.2	57 000	20–21
SiO_2	0.58×10^{-6}	1.47×10^{-2}	5000	88–89

$$\Delta T_{23} = T_2 - T_3 = \frac{Q}{h}, \tag{10}$$

$$\Delta T_3 = \frac{Q_t}{m c_s}. \tag{11}$$

Equation (9) is the well known Fourier relation for the heat flow in stationary condition between two surfaces placed at distance D in a medium of thermal conductivity k. In Eq. (10) h represents the heat transfer coefficient at the crystal-fluid surface. Finally, Eq. (11) describes the increase of the temperature of the cooling fluid, whose specific heat is c_s.

In order to obtain the equilibrium temperature of Si or SiO_2 mirror, we consider a water flow of 4.6 1/min which thus gives $h \cong 1$.[21] As the power density on M1 is very low, both ΔT_{23} and ΔT_3 can be neglected in Eq. (8). The only relevant term ΔT_{12} is then evaluated for both Si and SiO_2 by assuming a mirror thickness of 10 cm and an inlet fluid temperature of about 20 °C. In Table V we report the equilibrium temperatures and the induced radii of curvature R_t. The thermal curvature R_t of the Si mirror provides a slope of about 10 μrad. This value is compatible with those reported in the first row of Table IV which provide undistorted images (according to ray-tracing simulation). For the sake of completeness, we have also studied the effect of thermal distortion on the SiO_2 mirror.

The thermal distortion of mirror M1 has been introduced in the ray-tracing simulation of both layouts A and B. Several curved surfaces have been numerically prepared as inputs for SHADOW. The surfaces were generated by the following procedure. In the sagittal (meridional) plane of the mirror, we assumed that the equation for the curvature of the mirror surface is given by the superposition of the toroidal surface and of the cylindrical surface originated by the thermal load distortions. This equation can be written as

$$y = (R_1 - R_t) + -R_1\sqrt{1 - \frac{x^2}{R_1^2}} + R_t\sqrt{1 - \frac{x^2}{R_t^2}}, \tag{12}$$

where R_1 is the radius of curvature of the unperturbed surface in the sagittal (meridional) plane, and R_t is the radius induced by the thermal slope. Since the mirror dimensions are small with respect to R_1 and R_t, one can expand Eq. (12) in x/R, neglect the third order terms. The surface can then be rewritten as

$$y = \frac{x^2}{2}\left(\frac{1}{R_1} - \frac{1}{R_t}\right) = p x^2. \tag{13}$$

Consequently, when considering both meridional and sagittal planes, the original spherical surface of the undistorted mirror becomes a parabolic surface, whose equation is

This article is copyrighted as indicated in the article. Reuse of AIP content is subject to the terms at: http://scitationnew.aip.org/termsconditions. Downloaded to IP: 132.204.37.217 On: Wed, 10 Dec 2014 17:51:20

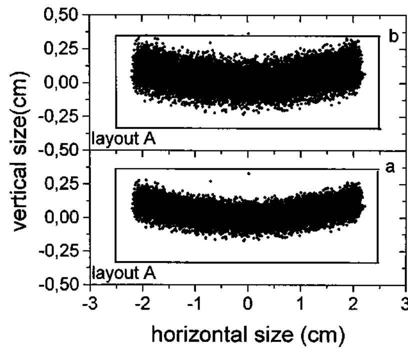

FIG. 11. Effect of the thermal curvature R_t of the mirror M1 on the image at the mask/wafer plane; (a) $R_t = 5000$ m, in (b) $R_t = 2500$ m. The box indicates the snout of the stepper.

$$z = p_1 x^2 + p_2 y^2. \tag{14}$$

The coefficients p_1 and p_2 are calculated from Eq. (13) using the curvature radius R_1 for the sagittal and the meridional planes, respectively.

Equation (14) can also be used for layout A, where M1 is a plane mirror, by setting $R_1 = \infty$. When including thermal distortions, M1 in practice becomes a cylindrical mirror, whose symmetry axis lies in the meridional plane. Figure 11 shows the images in the case of $R_t = 5000$ m [Fig. 11(a)] and $R_t = 2500$ m [Fig. 11(b)] for layout A. In both cases, neither the vertical nor the horizontal dimension of the image exceed the vertical size (6 mm) of the aperture slit of the stepper (snout).

For layout B, where M1 is toroidal, the distortions on the sagittal plane can be neglected, as the radius ρ is considerably smaller then R_t. Therefore, we have adopted the following expression for the M1 surface:

$$z = py^2 - \sqrt{\rho^2 - x^2} + \rho^2, \tag{15}$$

with

$$p = \frac{1}{2}\left(\frac{1}{R} - \frac{1}{R_t}\right). \tag{16}$$

Figure 12(a) represents the image obtained for layout B in the case of $R_t = 5000$ m, while in Fig. 12(b) is the image reported for $R_t = 2500$ m. In both cases [Figs. 12(a) and 12(b)] there is a clear increase in the number of lost rays due to an enlargement of the image. In conclusion, layout A turns out to be more stable than B, once thermal effects are taken into account.

Finally, we have applied the gray-body theory to the case of mirror M1 in order to evaluate its equilibrium temperature in the absence of cooling. We have considered a flat mirror of size $10 \times 65 \times 10\ \text{cm}^3$ made of silicon and contained in a stainless steel chamber. With $Q = 60$ W and $T_2 = 300$ K, we obtained from Eq. (5) $T_1 = 340$ K which corresponds to a value of R_t not acceptable by the optical design.

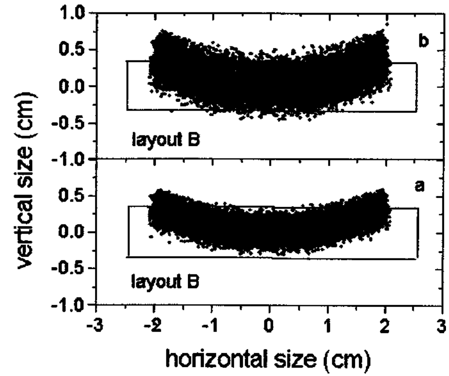

FIG. 12. Effect of the thermal curvature R_t of the mirror M1 on the image at the mask/wafer plane. (a) $R_t = 5000$ m, (b) $R_t = 2500$ m. The box indicates the snout of the stepper.

V. FIGURES OF MERIT OF THE BEAMLINE

In this section we evaluate three important parameters for the fabrication process using x-ray lithography; the resolution, the placement accuracy, and the throughput as a function of the beamline characteristics.

A. Resolution

In proximity lithography[23] the resolution has to be intended as the patterning ability, i.e., the capability to realize a given pattern under certain imaging conditions. In soft lithography one is interested in printing features whose size is smaller than 100 nm. In proximity imaging the resolution depends on many factors, such as the illumination system (source and beamline), the mask, and the interaction of the x rays with the resist material.

The following relation[24] links the characteristics of the optical system to the size δ of the smallest feature in the exposed pattern:

$$\delta = K_1 \sqrt{\lambda g}. \tag{17}$$

Here, λ is the average wavelength of the spectrum, g the distance between the mask and the wafer (gap distance), and K_1 is a factor given by the Rayleigh criterion.[25]

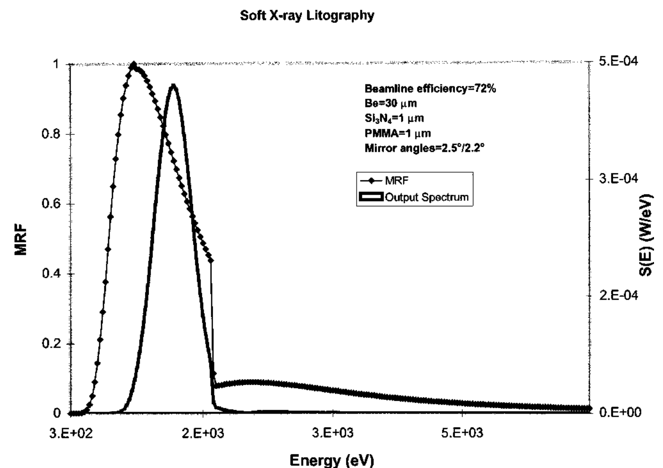

FIG. 13. The MRF function (full triangle) and the spectral band S of the beamline (continuous line) as calculated by TRANSMIT for soft x-ray lithography. The efficiency achieved is about 72%.

This article is copyrighted as indicated in the article. Reuse of AIP content is subject to the terms at: http://scitationnew.aip.org/termsconditions. Downloaded to IP: 132.204.37.217 On: Wed, 10 Dec 2014 17:51:20

It has been shown elsewhere[26] that $K_1 = 0.6$ may be obtained with an appropriate design of the beamline and of the x-ray mask. According to these results we expect $\delta \cong 50$ nm when $g = 10\,\mu$m in the soft lithography regime.

B. Placement accuracy

The beam placement accuracy depends on many factors, such as the beamline runout, the mask material, the x-ray exposure tool and the electron-beam mask writer. Here we consider the role of the beamline runout which is the only parameter relevant to the present study. As shown in Fig. 5 the runout of the beamline in the horizontal plane is limited within ± 1 mrad if one considers an exposure field of $2 \times 2\,\mathrm{cm}^2$. The vertical direction is not relevant as it is scanned by the beam. The resulting contribution to the placement accuracy is ± 10 nm for a gap of 10 μm. For deep lithography both the resolution and the placement accuracy are less critical due to the beamline performances and to the scattering processes in the substrate. In fact, in deep lithography the resolution ranges from a few microns to hundreds of microns, because increasing the depth, the resolution has to decrease due to the fabrication limit of the high aspect ratio of the structures. As a consequence, even the placement accuracy can be relaxed (the tolerance on the placement is $\approx 0.1\ \delta$).[27]

C. Throughtput

In order to evaluate the throughput figure of merit, one should discuss in some detail the efficiency of the beamline in different operating conditions. We define the efficiency as the ratio between the power delivered by the beamline and that absorbed by the resist material. In order to calculate this ratio, we utilize a mask-resist filter function (MRF function) that selects the part of radiation responsible of the image formation in the resist. All the radiation that is outside the ''lithographic window'' determined by the MRF is wasted and does not contribute to the lithographic process.

If the transmittance of the mask is $T(E)$ and the absorbance of the resist is $A(E)$ the MRF function is defined as:[28]

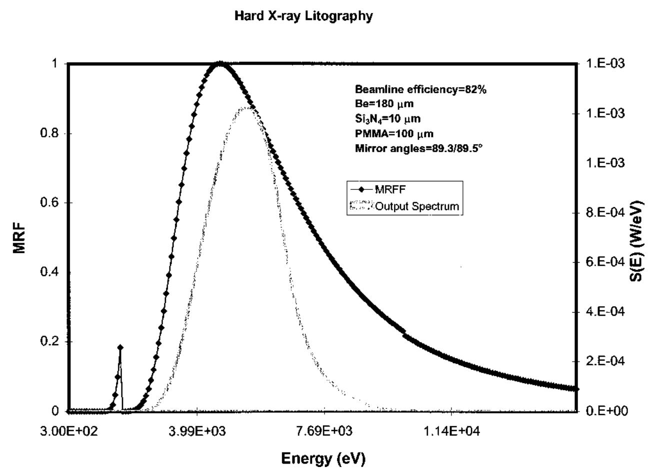

FIG. 14. The MRF function (full triangle) and the spectral band S of the beamline (continuous line) as calculated by TRANSMIT for hard x-ray lithography. The efficiency achieved is about 82%.

$$\mathrm{MRF}(E) = \frac{T(E)A(E)}{\max[\mathrm{MRF}(E)]}, \tag{18}$$

where $\max[\mathrm{MRF}(E)]$ is a normalization factor that guarantees a normalization equal to 1 for the $\mathrm{MRF}(E)$ function. If the beamline delivers a spectrum $S(E)$, the fraction of power R falling within the filters is

$$R = \int \mathrm{MRF}(E)S(E)dE. \tag{19}$$

The efficiency can then be defined as:

$$\eta = \frac{R}{\int S(E)dE}. \tag{20}$$

Figures 13 and 14 show the $\mathrm{MRF}(E)$ function and the spectral bandpass for soft and deep lithography. The optimized conditions for the mirror angles and the filter thickness are reported in the graphs. In both cases the efficiency is higher than 50%. This optimization can be reached at the cost of rejecting power. In our case we reached a good tradeoff between the efficiency and the absolute delivered power. The power fall for soft and deep lithography is reported in Table

TABLE VI. Downstream absorbed power on each optical element of layout A.

Ring parameters: energy: 2 GeV; source power: 86 W; beam current: 350 mA						
	Soft Lithography					
	Be No. 1 (thickness) 15 μm	Mirror No. 1 (angle) 2.5°	Mirror No. 2 (angle) 2.2°	Be No. 2 (thickness) 15 μm	Si_3N_4 (thickness) 2 μm	PMMA (thickness) 1 μm
Power after each optical element (W)	63.6	2.1	0.84	0.36	0.23	0.21
	Deep Lithography					
	Be No. 1 (thickness) 175 μm	Mirror No. 1 (angle) 0.3°	Mirror No. 2 (angle) 0.1°	Be No. 2 (thickness) 15 μm	Si_3N_4 (thickness) 10 μm	PMMA (thickness) 100 μm
Power after each optical element (W)	42.0	15.8	11.6	11.2	4.2	3.4

This article is copyrighted as indicated in the article. Reuse of AIP content is subject to the terms at: http://scitationnew.aip.org/termsconditions. Downloaded to IP: 132.204.37.217 On: Wed, 10 Dec 2014 17:51:20

VI. For soft x rays, for example, a typical threshold dose density is 100 mJ/cm^2. One can expose in this case, an area of 2×2 cm^2 in 1 s. For deep lithography the delivered power is higher by more than one order of magnitude than soft lithography, as the layer of resist to be exposed is 100 μm thick.

VI. DISCUSSION

In this article we have presented a comparative study of two beamline configurations and two typical mirror materials for an x-ray lithography beamline at ELETTRA. Their peculiarity lie in a wide lithographic window, which is accessible to both soft and hard x rays. Both designs give the possibility of performing high resolution and deep lithography with the same beamline. Layout B gives a better performance than layout A in terms of placement accuracy because the horizontal beam divergence is about 1 mrad less than that with layout A. Nevertheless, we chose to implement layout A at ELETTRA because the lithographic performance is less sensitive to the thermal load of the mirrors, still preserving a high resolution capability at soft x-ray regime. The study includes an evaluation of all the optical parameters that affect the beam quality and the lithography, such as, thermal load on filters and mirrors, slope errors, mirror coating roughness, lithographic efficiency, and throughput.

The resolution, the placement accuracy, and the throughput are optimized to be compatible in the soft x-ray regime, with a feature printability well below 100 nm.

ACKNOWLEDGMENTS

The authors would like to thank Professor P. Calvani for critically reading the manuscript. We also thank Professor F. Cerrina and Professor L. Braikovich for many useful suggestions. We are also indebted to Dr. S. Sangeet, Dr. Manolo Sanchez del Rioand, and Dr. Filippo Romanato. This work was supported by ''Progetto LILIT'' of INFM of Italy.

[1] G. Margaritondo, A. Savoia, and A. Wrulich, Sci. Am. (Le Scienze) **342**, 32 (1997).
[2] J. Xiao, F. Cerrina, and R. Rippstein, J. Vac. Sci. Technol. B **12**, 4018 (1994).
[3] H. Sumitani, K. Itoga, M. Inowe, H. Watanabe, N. Yamamoto, and Y. Matsui, Proc. SPIE **2437**, 94 (1995).
[4] H. Ban, J. Nakamura, K. Deguchi, and A. Tanaka, J. Vac. Sci. Technol. B **12**, 3904 (1994).
[5] E. Di Fabrizio, M. Gentili, L. Grella, M. Baciocchi, A. Krasnoperova, F. Cerrina, W. Yun, B. Lai, and E. Gluskin, J. Vac. Sci. Technol. B **12**, 3979 (1994).
[6] W. Ehrfeld, V. C. Gartner, Golbig, V. Hessel, R. Konrad, H. Lowe, T. Richter, and C. Shulz *Proceedings of the First Conference on Microreaction Technology* (Springer, Berlin, 1998), pp. 72–90.
[7] G. Feiertag and W. Ehrfeld Appl. Phys. Lett. **71**, 1441 (1997).
[8] K. Makoto, Kamigori-cho, Ako-Gun, and K. Tomohiko, European Patent Application No. 95116295.7 (1996).
[9] R. Rinaldi, C. Turco, N. Lovergine, R. Cingolani, L. Vasanelli, E. Di Fabrizio, M. Gentili, L. Grella, L. Decaro, and L. Tapfer, Appl. Phys. Lett. **71**, 3770 (1997).
[10] J. D. Joannopoulos, R. D. Meade, and J. N. Winn, *Photonic Crystal* (Princeton University Press, Princeton, NJ, 1995).
[11] R. Cole and F. Cerrina, Proc. SPIE **1465**, 111 (1991).
[12] F. De Carlo, D. C. Mancini, and B. Lai, Microsyst. Technol. **4**, 86 (1998).
[13] C. Welnak, G. J. Chen, and F. Cerrina, Nucl. Instrum. Methods Phys. Res. A **347**, 344 (1994).
[14] ELETTRA WEB site at www.elettra.trieste.it.
[15] S. Goto, T. Taguchi, T. Osada, S. Okamura, and T. Hisatsugu, J. Vac. Sci. Technol. B **12**, 286 (1993).
[16] K. Simon, R. Leonard, and F. Cerrina, Micro. Nanocircuit Eng. (to be published).
[17] A. K. Freund, F. De Bergeuin, G. Marot, C. Riekel, S. Susini, L. Zhang, and E. Ziegler, Opt. Lett. **29**, 928 (1990).
[18] M. Sanchez del Rio and A. Marcelli, Nucl. Instrum. Methods Phys. Res. A **319**, 170 (1992).
[19] F. Cerrina, Internal Report No. 2, 1988 at CXRL (Center for X-Ray Lithography) 3731 Schneider Dr., Stoughton, WI.
[20] F. Kreith, *Principles of Heat Transfer* (Dun-Donnelley, New York, 1973).
[21] R. K. Smither, Nucl. Instrum. Methods Phys. Res. A **291**, 286 (1990).
[22] Brush Wellman, Enginnered Materials Catalog, 34325 Ardenwood Blvd., Fremont, CA 94555.
[23] J. Guo and F. Cerrina, IBM J. Res. Dev. **37**, 331 (1993).
[24] J. Guo, Q. Leonard, F. Cerrina, E. Di Fabrizio, L. Luciani, M. Gentili, and D. Gerold, J. Vac. Sci. Technol. B **10**, 3150 (1992).
[25] J. W. Goodman, *Introduction to Fourier Optics* (McGraw-Hill, New York, 1968).
[26] M. Gentili, E. Di Fabrizio, L. Grella, M. Baciocchi, L. Mastrogiacomo, R. Maggiora, J. Xiao, and F. Cerrina, J. Vac. Sci. Technol. B **12**, 3954 (1994).
[27] M. Fukuda, M. Suzuki, M. Kanai, H. Tsuyuzaki, A. Shibayama, and S. Ishihara, J. Vac. Sci. Technol. B **12**, 3256 (1994).
[28] M. Khan, L. Mohammad, L. Ocola, J. Xiao, and F. Cerrina, J. Vac. Sci. Technol. B **12**, 3930 (1994).

This article is copyrighted as indicated in the article. Reuse of AIP content is subject to the terms at: http://scitationnew.aip.org/termsconditions. Downloaded to IP: 132.204.37.217 On: Wed, 10 Dec 2014 17:51:20